
This is an electronic reprint of the original article.
This reprint may differ from the original in pagination and typographic detail.

Pushkarev, Alexander B.; Kovalev, Y. Y.; Lister, M. L.; Savolainen, T.

MOJAVE - XIV. Shapes and opening angles of AGN jets

Published in:
Monthly Notices of the Royal Astronomical Society

DOI:
[10.1093/mnras/stx854](https://doi.org/10.1093/mnras/stx854)

Published: 01/07/2017

Document Version
Publisher's PDF, also known as Version of record

Please cite the original version:
Pushkarev, A. B., Kovalev, Y. Y., Lister, M. L., & Savolainen, T. (2017). MOJAVE - XIV. Shapes and opening angles of AGN jets. *Monthly Notices of the Royal Astronomical Society*, 468(4), 4992-5003.
<https://doi.org/10.1093/mnras/stx854>

This material is protected by copyright and other intellectual property rights, and duplication or sale of all or part of any of the repository collections is not permitted, except that material may be duplicated by you for your research use or educational purposes in electronic or print form. You must obtain permission for any other use. Electronic or print copies may not be offered, whether for sale or otherwise to anyone who is not an authorised user.

MOJAVE – XIV. Shapes and opening angles of AGN jets

A. B. Pushkarev,^{1,2★} Y. Y. Kovalev,^{2,3} M. L. Lister⁴ and T. Savolainen^{5,6,3}

¹Crimean Astrophysical Observatory, Nauchny 298409, Crimea, Russia

²Astro Space Center of Lebedev Physical Institute, Profsoyuznaya 84/32, Moscow 117997, Russia

³Max-Planck-Institut für Radioastronomie, Auf dem Hügel 69, D-53121 Bonn, Germany

⁴Department of Physics, Purdue University, 525 Northwestern Avenue, West Lafayette, IN 47907, USA

⁵Aalto University Metsähovi Radio Observatory, Metsähovintie 114, FI-02540 Kylmälä, Finland

⁶Aalto University Department of Electronics and Nanoengineering, PL 15500, FI-00076 Aalto, Finland

Accepted 2017 April 4. Received 2017 March 12; in original form 2017 January 9

ABSTRACT

We present 15 GHz stacked VLBA images of 373 jets associated with active galactic nuclei (AGNs) having at least five observing epochs within a 20 yr time interval 1994–2015 from the Monitoring Of Jets in Active galactic nuclei with VLBA Experiments (MOJAVE) programme and/or its precursor, the 2-cm VLBA Survey. These data are supplemented by 1.4 GHz single-epoch VLBA observations of 135 MOJAVE AGNs to probe larger scale jet structures. The typical jet geometry is found to be close to conical on scales from hundreds to thousands of parsecs, while a number of galaxies show quasi-parabolic streamlines on smaller scales. A true jet geometry in a considerable fraction of AGNs appears only after stacking epochs over several years. The jets with significant radial accelerated motion undergo more active collimation. We have analysed total intensity jet profiles transverse to the local jet ridgeline and derived both apparent and intrinsic opening angles of the flows, with medians of 21°5 and 1°3, respectively. The *Fermi* LAT-detected gamma-ray AGNs in our sample have, on average, wider apparent and narrower intrinsic opening angle, and smaller viewing angle than non-LAT-detected AGNs. We have established a highly significant correlation between the apparent opening angle and gamma-ray luminosity, driven by Doppler beaming and projection effects.

Key words: galaxies: active – BL Lacertae objects: general – galaxies: jets – quasars: general.

1 INTRODUCTION

The current understanding of the phenomenon of active galactic nuclei (AGNs) suggests that accretion of matter on to black holes with masses up to $M_{\text{bh}} \sim 10^{10} M_{\odot}$ is converted into kinetic energy of highly collimated bipolar outflows of plasma along the rotation axis of the black hole or accretion disc. The jets are formed in the immediate vicinity of the central engine and become detectable at distances of a few tens of gravitational radii ($R_g = GM_{\text{bh}}/c^2$) at millimeter wavelengths (Junor, Biretta & Livio 1999; Hada et al. 2011). At scales of 10^3 – $10^5 R_g$, the outflows are accelerated to relativistic speeds, as follows from the apparent superluminal motions (Lister et al. 2016), high Doppler factors (Hovatta et al. 2009) and extreme brightness temperatures that may significantly exceed the limit of 10^{12} K set by inverse Compton cooling (Kellermann & Pauliny-Toth 1969). The jets can propagate up to megaparsec scales, where they become diffuse while interacting with the intergalactic

medium. The nature of the processes and the physical conditions that govern forming, accelerating and collimating these relativistic jets remain among the most challenging problems of contemporary astrophysics.

By now, jet shapes have been studied only for a very limited number of nearby sources, such as M87 (Asada & Nakamura 2012), Mkn 501 (Giroletti et al. 2008), Cygnus A (Boccardi et al. 2016), NGC 6251 (Tseng et al. 2016), NGC 1052 (Kadler et al. 2004), 3C 66A (Böttcher et al. 2005) and 3C 84 (Savolainen, private communication) to probe the innermost jet regions. In Pushkarev et al. (2009), we analysed the opening angles of 142 AGN jets, based on single-epoch VLBA data. These AGNs were drawn from the Monitoring Of Jets in Active galactic nuclei with VLBA Experiments (MOJAVE) radio flux density-limited sample referred to as MOJAVE-1 (Lister et al. 2009a) and an accompanying gamma-ray selected sample (Lister et al. 2011). Here, we present opening angle analysis of a larger sample comprising 373 AGNs, together with the first systematic study of jet shapes on parsec scales using multi-epoch VLBA observations at 15 GHz and on larger scales probed by single-epoch VLBA observations at 1.4 GHz of the MOJAVE-1 sources.

* E-mail: pushkarev.alexander@gmail.com

Table 1. Source properties. Columns are as follows: (1) B1950 name; (2) J2000 name; (3) other name; (4) *Fermi* gamma-ray association name; (5) optical class, where B = BL Lac, Q = quasar, G = radio galaxy, N = narrow-lined Seyfert 1 and U = unidentified; (6) MOJAVE 1.5 Jy sample membership flag; (7) redshift; and (8) reference for redshift and/or optical classification. This table is available in its entirety in the online journal. A portion is shown here for guidance regarding its form and content.

B1950 (1)	J2000 (2)	Alias (3)	Gamma-ray association. (4)	Optical class (5)	1.5 Jy (6)	z (7)	Reference (8)
0003+380	J0005+3820	S4 0003+38	3FGL J0006.4+3825	Q	–	0.229	Stickel & Kuehr (1994)
0003–066	J0006–0623	NRAO 005	–	B	Y	0.3467	Jones et al. (2005)
0006+061	J0009+0628	CRATES J0009+0628	3FGL J0009.1+0630	B	–	–	Rau et al. (2012)
0007+106	J0010+1058	III Zw 2	–	G	Y	0.0893	Sargent (1970)
0010+405	J0013+4051	4C +40.01	–	G	–	0.256	Thompson et al. (1992)
0011+189	J0013+1910	RGB J0013+191	2FGL J0013.8+1907	B	–	0.477	Shaw et al. (2013)
0015–054	J0017–0512	PMN J0017–0512	3FGL J0017.6–0512	Q	–	0.226	Shaw et al. (2012)
0016+731	J0019+7327	S5 0016+73	–	Q	Y	1.781	Lawrence et al. (1986)
0019+058	J0022+0608	PKS 0019+058	3FGL J0022.5+0608	B	–	–	Shaw et al. (2013)
0026+346	J0029+3456	B2 0026+34	–	G	–	0.517	Zensus et al. (2002)

This paper is part of a series based on data from the MOJAVE programme¹ to monitor radio brightness and polarization variations in jets associated with active galaxies with declinations above -30° . The earlier papers have focused on the parsec-scale kinematics of the jets (Lister et al. 2009b, 2013, 2016), their acceleration and collimation (Homan et al. 2009, 2015), spectral distributions (Hovatta et al. 2014), nuclear opacity (Pushkarev et al. 2012), Faraday rotation (Hovatta et al. 2012), parent luminosity function (Cara & Lister 2008), relativistic beaming and the intrinsic properties (Cohen et al. 2007), kiloparsec scale morphology (Cooper, Lister & Kochanzyk 2007) and circular and linear polarization (Homan & Lister 2006; Lister & Homan 2005).

The structure of this paper is as follows: In Section 2, we describe our observational data, source sample, stacking procedure and statistics of the stacked images; in Section 3, we discuss our results; and our main conclusions are summarized in Section 4. We use the term ‘core’ as the apparent origin of AGN jets, which commonly appears as the brightest feature in very long baseline interferometry (VLBI) images of blazars (e.g. Lobanov 1998). We adopt a cosmology with $\Omega_m = 0.27$, $\Omega_\Lambda = 0.73$ and $H_0 = 71 \text{ km s}^{-1} \text{ Mpc}^{-1}$ (Komatsu et al. 2009).

2 OBSERVATIONAL DATA

2.1 MOJAVE programme and 2-cm VLBA survey data. Stacked images

For the purposes of our study, we made use of data at 15 GHz from the MOJAVE programme, the 2-cm VLBA Survey (Kellermann et al. 1998; Zensus et al. 2002), and the National Radio Astronomy Observatory (NRAO) data archive for those sources that have at least five VLBA observing epochs between 1994 August 31 and 2015 August 20 inclusive. In total, this produced a pool of 370 AGNs, 8 of which were excluded due to uncertainty with regards to the core component location at some/all epochs, resulting in a final sample of 362 sources with 6461 VLBA maps at 735 individual epochs. These AGNs are members of the radio flux-density limited MOJAVE-1 (Lister et al. 2009a) and MOJAVE 1.5 Jy (Lister et al. 2015) samples, and gamma-ray flux limited and low-luminosity samples discussed by Lister et al. (2013). Also included is a set of weaker radio AGNs associated with gamma-ray hard

spectrum AGNs. The compact radio flux density of all sources from these samples is greater than 0.1 Jy at 15 GHz. Each of the final single-epoch images was constructed by applying natural weighting to the visibility function. For a more detailed discussion of the data reduction and imaging process schemes, see Lister et al. (2009a). The sample of 362 sources is strongly dominated by flat spectrum radio quasars (67 per cent) and BL Lacertae objects (24 per cent), but also contains 19 radio galaxies, 5 narrow-lined Seyfert 1 galaxies and 5 optically unidentified sources. The redshifts are currently known for 331 objects (91 per cent) ranging from $z_{\min} = 0.00436$ for the galaxy 1228+126 (M87) to $z_{\max} = 4.715$ for the quasar PKS 0201+113, with a mean value of the distribution close to $z = 1$. The general characteristics of the sources such as object name, its alternative name, gamma-ray association name, optical class, membership of flux density-limited MOJAVE 1.5 Jy sample and redshift are listed in Table 1.

Recently, Lister et al. (2013) found that nearly all of the 60 most heavily observed jets over a decade time interval within the MOJAVE/2-cm VLBA surveys displayed significant changes in their innermost jet position angle with time, suggesting that the superluminal AGN jet features seen in single-epoch images occupy only a portion of the entire jet cross-section. Thus, to better reconstruct the jet morphology, for each source we produced a corresponding stacked image using all available epochs from the MOJAVE/2-cm VLBA surveys at 15 GHz convolved with a circular beam based on the median beam size for the source, the same pixel size (0.1 mas) and field of view. The stacking procedure was performed as a simple averaging in the image plane after aligning single-epoch total intensity maps by the VLBI core position. The VLBI core position was derived from the structure modelling in the (u, v) domain with the procedure *modelfit* in the Caltech DIFMAP package (Shepherd 1997). For the model fitting, Lister et al. (2013, 2016) used a minimum number of circular (and in some cases elliptical) two-dimensional Gaussian components that after being convolved with the restoring beam, adequately reproduce the constructed brightness distribution of a source.

The distribution of total observing epochs used in each stacked image is quite broad, ranging from the minimum accepted 5 epochs up to 137 epochs (for BL Lac), with a median value of 11. The distribution of time range in a stacked map (Fig. 1) shows two humps representing two groups of sources dominated by following: (i) gamma-ray-bright objects listed as high-confidence associations by *Fermi*-LAT after 2008 (Acero et al. 2015); and (ii) long-term monitored AGNs belonging to both the 2-cm VLBA Survey and

¹ <http://www.astro.purdue.edu/MOJAVE>

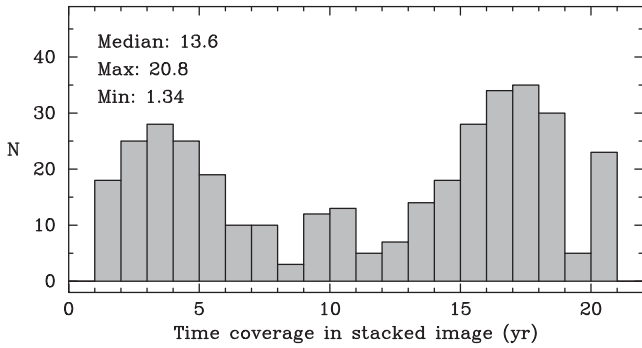


Figure 1. Histograms of time interval between first and last epochs in stacked images of 362 sources.

MOJAVE programme. The quasar 1928+738 (4C +73.18) has the longest (20.8 yr) observed time interval in our sample. We list the parameters of the stacked images in Table 2. The typical full width at half-maximum (FWHM) dimension of the circular restoring beam of the stacked VLBA images is about 0.8 mas, corresponding to a linear scale of ~ 6 parsecs in projection at the typical redshifts of

our sample ($z \simeq 1$). The stacking procedure effectively decreases the rms noise of the resulting image, on average, by a factor of few compared to that of single-epoch maps. The noise level was calculated as a minimum of rms estimates in four corner quadrants of the image, each of 1/16 of the image size. For most sources the bottom contour is shown at four times the rms level. The dynamic range of the images (determined as a ratio of the peak flux density to the rms noise level) ranges from 620 (weak galaxy 0026+346) to 92000 (BL Lac) with a median of $\sim 11\,500$. The typical rms noise level is ~ 0.06 mJy beam $^{-1}$. In Fig. 2, we show stacked images of three sources having the minimum (5), median (11) and maximum (137) number of epochs.

2.2 22-cm VLBA data

In addition to the 2-cm MOJAVE VLBA data, we made use of single-epoch longer wavelength VLBA observations of 135 MOJAVE-1 sources that constitute a statistically complete, flux-density limited sample. A total of 9 24-hour observing sessions during 2010 were carried out by D. Gabuzda et al. in full dual-polarization mode at four wavelengths in the range of 18–22 cm at an aggregate recording

Table 2. Summary of 15 GHz stacked image parameters. Columns are as follows: (1) B1950 name; (2) other name; (3) date of first epoch; (4) time range between first and last epochs; (5) number of stacked epochs; (6) FWHM of restoring beam (milliarcseconds); (7) I peak of image (Jy per beam); (8) rms noise level of image (mJy per beam); and (9) bottom I contour level (mJy per beam). This table is available in its entirety in the online journal. A portion is shown here for guidance regarding its form and content.

Source	Alias	First epoch (yyyy/mm/dd)	τ (yr)	N	Beam (mas)	I_{peak} (Jy beam $^{-1}$)	rms (mJy beam $^{-1}$)	I_{base} (mJy beam $^{-1}$)
(1)	(2)	(3)	(4)	(5)	(6)	(7)	(8)	(9)
0003+380	S4 0003+38	2006/03/09	7.42	10	0.70	0.460	0.07	0.29
0003-066	NRAO 005	1995/07/28	17.27	27	0.84	1.248	0.09	0.35
0006+061	CRATES J0009+0628	2011/12/29	1.43	5	0.86	0.150	0.09	0.37
0007+106	III Zw	1995/07/28	17.85	25	0.79	0.740	0.07	0.27
0010+405	4C +40.01	2006/04/05	5.22	12	0.70	0.507	0.03	0.11
0011+189	RGB J0013+191	2013/12/15	1.42	6	0.79	0.104	0.03	0.10
0015-054	PMN J0017-0512	2009/07/05	4.01	8	0.83	0.231	0.04	0.17
0016+731	S5 0016+73	1994/08/31	16.07	15	0.70	0.951	0.11	0.45
0019+058	PKS 0019+058	2014/02/14	1.34	5	0.78	0.275	0.03	0.12
0026+346	B2 0026+34	1995/04/07	9.24	7	0.88	0.087	0.14	0.56

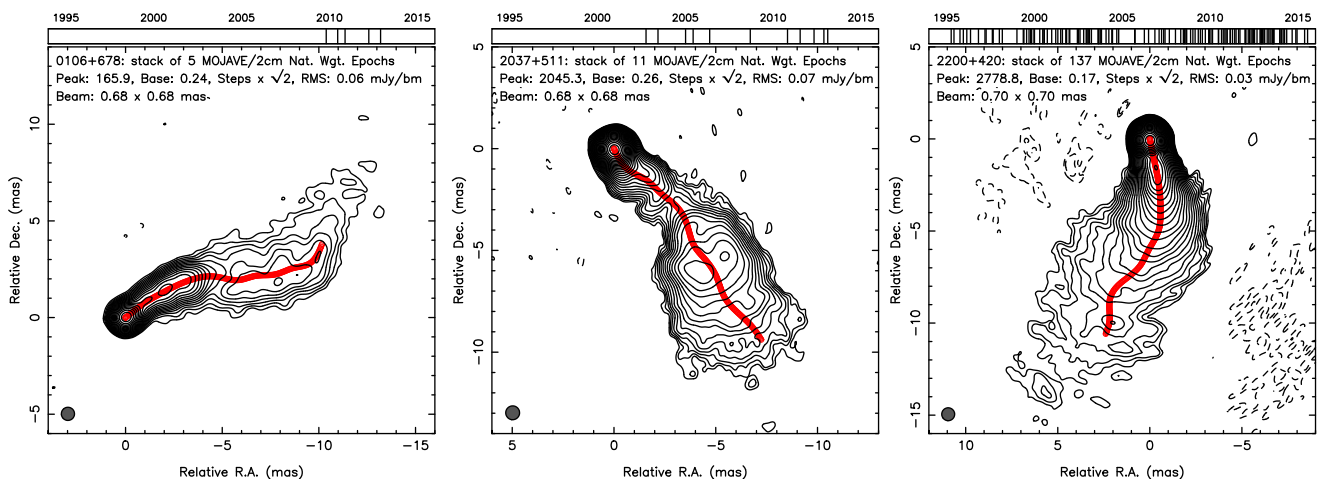


Figure 2. Examples of 15 GHz naturally weighted stacked CLEAN images of observed sources with minimum (5), median (11) and maximum (137) number of epochs. The contours are plotted at increasing powers of $\sqrt{2}$. The restoring beam is depicted, as a shaded circle in the lower left corner. The constructed total intensity ridgeline is shown by red. A wedge indicating observing epochs (vertical ticks) used for producing the stacked image is shown on top. The 15 GHz VLBA contour stacked images of all 362 sources with constructed ridgelines are available in the online journal.

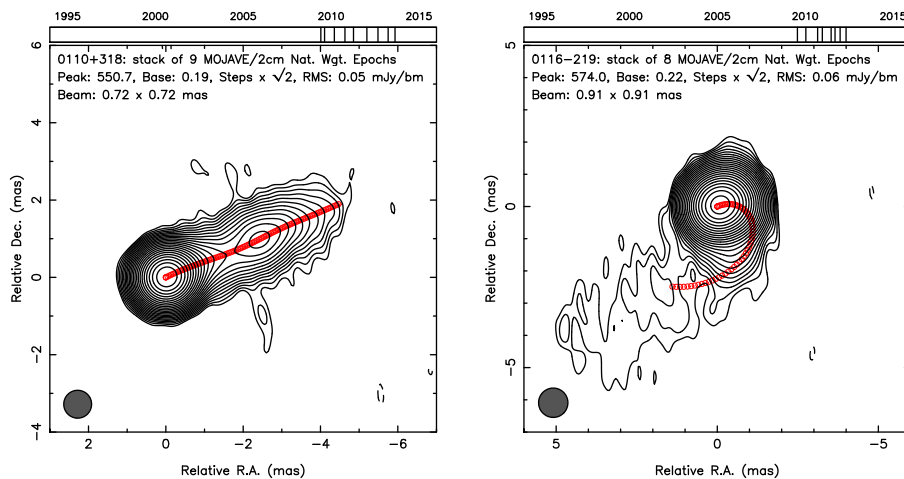


Figure 3. Examples of nearly straight (left-hand panel) and significantly curved (right-hand panel) jets. The contours are plotted at increasing powers of $\sqrt{2}$. The restoring beam is depicted, as a shaded circle in the lower left corner. The constructed total intensity ridgeline is shown by red. A wedge indicating observing epochs used for producing the stacked image is shown on top.

bit rate of 256 Mbits s^{-1} . The L-band project was originally aimed on studying Faraday rotation properties across the jet.² We have processed and imaged the data at the longest wavelength, 22 cm, to reconstruct the outer total intensity jet structure and probe large scales that can extend to 100 mas or more.

3 RESULTS

3.1 Total intensity ridgelines

In our earlier study (Pushkarev et al. 2009), we approximated the jet axis by a straight line for relatively unbroken morphology or by two connected lines for sources with notably bending outflows. In the current analysis, we have constructed total intensity ridgelines to follow the jet more accurately. The ridge-finding procedure adopts a polar coordinate system centred on the core and uses an azimuthal slice to find the weighted average, i.e. the point where the intensity integrated along the arc is equal on the two sides excluding the pixels with low-SNR (< 8 times rms). The algorithm advances down the jet for successively increasing radial values. Finally, the ridgeline is constructed by fitting a cubic spline and interpolating it at roughly equal intervals (0.05 mas) of radial distance (Fig. 2). As the procedure operates in the image plane, an elongated restoring beam could affect the ridgeline, forcing it to the direction of the major axis. Therefore, all the stacked images were made from single-epoch maps convolved with a median circular beam. For the sources with two-sided jet morphology, for example, NGC 1058, 3C 84 and 1413+135, we set corresponding azimuth limits to reconstruct the ridgeline of the approaching jet only.

The path lengths along the constructed ridgelines range from 1 to 57 mas, with a median of about 6 mas. Due to jet bending being magnified by projection effects, the ridgeline path length is always larger than the radial distance from the core to ridgeline final point. The ratio of these values is close to 1 for straight jets and reaches up to 1.8 for the highly curved outflow of the quasar 0116–219, which has a continuous change of the ridgeline position angle exceeding 200° (Fig. 3). The quasar 2135+141 is known for its extremely bent

jet with $\Delta\text{PA} = 210^\circ$ on scales probed by 2–43 GHz VLBI observations (Savolainen et al. 2006), and shows a total position angle change of about 150° in the 15 GHz stacked image. On average, the standard deviation of jet position angle is inversely proportional to jet length r , following the median dependence $\sigma_{\text{PA}[\text{deg}]} = 7.4/r_{[\text{mas}]}$.

3.2 Jet shapes

We used the 15 GHz total intensity MOJAVE stacked images and constructed ridgelines to study the shapes of the outflows. Moving down the ridgeline, we made slices transverse to the local jet direction. The slices were taken at 0.05 mas intervals along the ridgeline, starting from the position of the core. For each cut, we obtained the FWHM D of a Gaussian fitted to the transverse jet brightness profile and the corresponding deconvolved jet width $d = (D^2 - b^2)^{1/2}$, where b is the FWHM size of the restoring beam. We analysed a dependence between the jet width d and path length r measured along the reconstructed total intensity ridge line. We fit an assumed single power-law dependence $d \propto r^k$ using the least squares method through all the distances $r > 0.5$ mas. The data points were initially smoothed by five-point moving averaging. In Fig. 4, we show this dependence for BL Lac, as an example. The width errors were estimated by deviating a position angle of the transverse jet cut in a range $\pm 15^\circ$ with a step of 1° and calculating the rms.

Distributions of the power-law index k (Fig. 5, top three panels) were constructed separately for sources of different spectral classes. BL Lacs and quasars typically show jet shape close to conical (i.e. $k = 1$), although BL Lacs tend to have, on average, larger k -indices than those of quasars, with medians of 0.98 and 0.85, respectively. Galaxies are characterized by lower k -index values, with a median of 0.68, suggesting that in a number of cases the jet profile is close to parabolic geometry, as for example, in M87 for which $k = 0.45$ that is in agreement with other VLBI jet shape studies of M87 (Asada & Nakamura 2012; Hada et al. 2013, 2016). Most probably, this is a result of their proximity and larger viewing angle, allowing us to probe smaller physical scales closer to the jet apex. A jet shape transition from parabolic to conical detected in a few sources will be discussed in a separate paper (Kovalev et al., in preparation.). A dependence between k -index and redshift is significant if galaxies and BL Lacs are considered only, and becomes non-significant for quasars only. The distribution for all sources (Fig. 5, bottom panel)

² http://www.physics.ucc.ie/radiogroup/18-22cm_observations.html

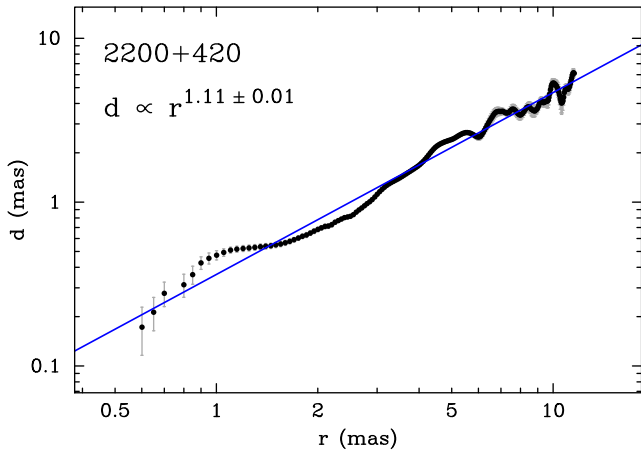


Figure 4. Transverse jet width versus a distance along ridge line for BL Lac at scales probed by the MOJAVE observations at 15 GHz. The thick blue line is the best fit of an assumed power-law dependence $d \propto r^k$. The plots for other sources are available in the online journal.

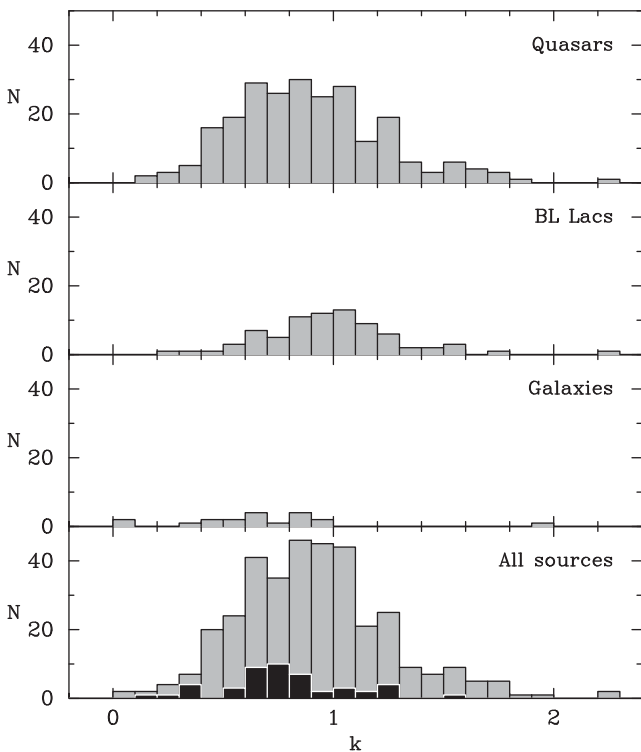


Figure 5. Histograms of the power-law index k in $d \propto r^k$ fitted dependence for 238 quasars, 78 BL Lacs, 19 galaxies, and all sources together. Black bins represent sources with radial accelerated motion detected in their jets.

has a median of 0.89. This is consistent with the median k -index of 0.8 derived from results of model fitting performed in the (u, v) plane for a small sample of 30 sources observed at 8.6 GHz with global VLBI (Pushkarev & Kovalev 2012).

The overlaid black bins show sources with positive or negative radial accelerated motion observed in their jets (Homan et al. 2015). These objects have statistically a lower k parameter compared to that of the rest of sources, with medians of 0.73 and 0.91, respectively, reflecting that the outflows with accelerated motion undergo more active collimation.

We tested the robustness of the obtained results by progressively cutting the ridgeline length r down to 1 mas from the core and repeating the analysis with the sub-data sets. The corresponding median k -index values remain constant until the ridgeline is up to 10 mas long, while for shorter ridgelines the median gradually increases, peaking up to 1.0 at $r = 1.2$ mas. We explain this by a non-uniform degree of completeness of jet cross-section that can decrease beyond a certain distance from the VLBI core. This is because the source brightness distribution is stacked over a limited time interval that might be not long enough for jet features emergent at different position angles to propagate all the way down to distances where jet emission is detected in the stacked image. At the same time, the difference between the accelerated and non-accelerated sources also holds for all the data subsets. An observational bias that can also affect the k -index measurements to some degree is that there is a maximum angular scale to which the VLBA is sensitive. It is about $0.5\lambda/B_{\min}$, where λ is the wavelength of observation and $B_{\min} \approx 236$ km is the minimum baseline length (between the antennas Los Alamos and Pie Town, New Mexico). This corresponds to the scale of about 9 mas at 2 cm, while about 75 per cent of sources in our sample manifest jet structure on smaller scales, making this bias weak.

3.2.1 Larger scales at 1.4 GHz

Due to a steep spectrum of the jet synchrotron emission, with a typical spectral index -0.7 measured between 2 and 8 GHz (Pushkarev & Kovalev 2012) and -1.0 between 8 and 15 GHz (Hovatta et al. 2014), observations at lower frequencies probe larger scales of the outflows, can be used to effectively reconstruct the jet cross-section even with single-epoch data. Using the VLBA observations at 1.4 GHz, we imaged jet structure on scales roughly one order of magnitude larger than those at 15 GHz, extending to 100 mas or more (Fig. 6, left-hand panel, middle panel). Typical dynamic range of the images is about 3900, with a median noise level of about 0.3 mJy beam $^{-1}$. We list the parameters of the single-epoch 1.4 GHz total intensity images in Table 3. Out of 135 observed sources, we constructed total intensity ridgelines using the procedure described in Section 3.1 for 122 with a clear core-jet morphology, omitting the sources that are either too compact or have unclear core position. One source, the quasar 2005+403, seen through the turbulent Cygnus region, is found to be heavily scattered (Fig. 6, right-hand panel).

Another aspect of the low-frequency observations is that the absolute position of the VLBI core at 1.4 GHz is expected to be shifted down the jet with respect to the 15 GHz core position mainly due to synchrotron self-absorption (e.g. Lobanov 1998; Sokolovsky et al. 2011; Kutkin et al. 2014; Kravchenko et al. 2016). The magnitude of the core shift effect between 15 and 1.4 GHz can be estimated using a typical value of 0.13 mas derived statistically between 15 and 8 GHz (Pushkarev et al. 2012) or 0.44 mas between 8 and 2 GHz (Kovalev et al. 2008) and assuming that a separation of the VLBI core from the jet apex varies with frequency as $r_{\text{core}} \propto \nu^{-1}$. This yields a shift of the order of 1 mas, which is consistent with typical core shift 1.2 mas between 1.4 and 15 GHz measured by Sokolovsky et al. (2011) for a sample of 20 sources. The core shifts for individual sources in our sample cannot be derived from the single-epoch 1.4 GHz images and 15 GHz stacked maps since the stacking procedure smooths the temporally evolving source brightness distribution. Moreover, the core shift can vary significantly, especially during flares (Plavin et al., in preparation.). Therefore,

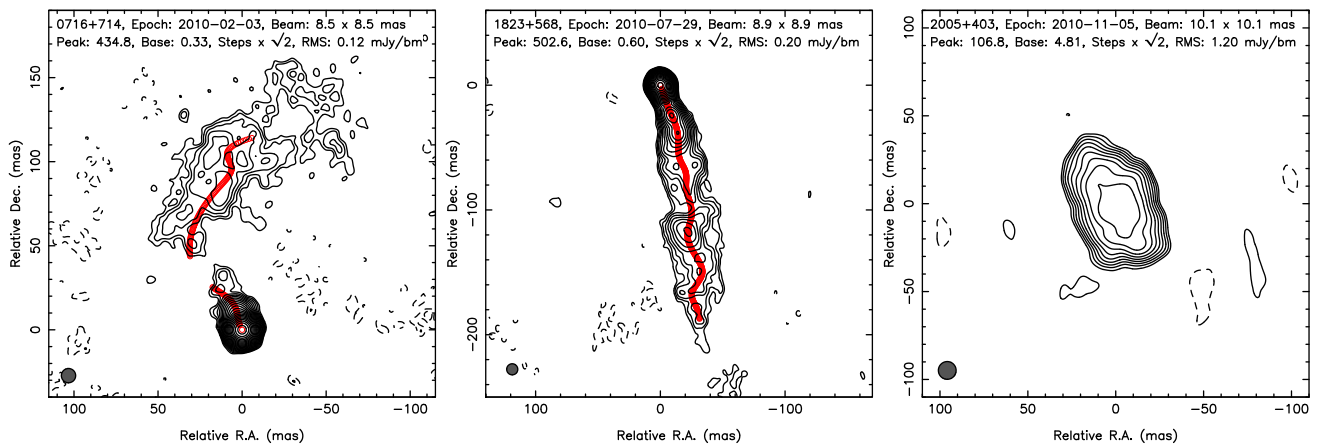


Figure 6. Examples of 1.4 GHz naturally weighted CLEAN images showing rich jet structure on scales of 100 mas or more (left-hand panel and middle panel) and a scattered source observed through the highly turbulent Cygnus region. The contours are plotted at increasing powers of $\sqrt{2}$. The restoring beam is depicted as a shaded circle in the lower left corner. The constructed total intensity ridgeline is shown by red. The 1.4 GHz VLBA contour images of 122 MOJAVE sources with constructed ridgelines are available in the online journal.

Table 3. Summary of 1.4 GHz single-epoch image parameters. Columns are as follows: (1) B1950 name; (2) other name; (3) observing epoch; (4) FWHM of restoring beam (milliarcseconds); (5) I peak of image (Jy per beam); (6) rms noise level of image (mJy per beam); and (7) bottom I contour level (mJy per beam). This table is available in its entirety in the online journal. A portion is shown here for guidance regarding its form and content.

Source	Alias	Epoch (yyyy/mm/dd)	Beam (mas)	I_{peak} (Jy beam $^{-1}$)	rms (mJy beam $^{-1}$)	I_{base} (mJy beam $^{-1}$)
(1)	(2)	(3)	(4)	(5)	(6)	(7)
0003–066	NRAO 005	2010/11/05	14.4	1.983	0.48	1.90
0016+731	S5 0016+73	2010/11/05	8.7	0.314	0.11	0.44
0048–097	PKS 0048–09	2010/06/18	13.5	0.218	0.13	0.50
0059+581	TXS 0059+581	2010/07/29	9.5	0.682	0.18	0.73
0106+013	4C +01.02	2010/08/23	13.4	1.445	0.36	1.44
0109+224	S2 0109+22	2010/09/23	11.6	0.209	0.09	0.35
0119+115	PKS 0119+11	2010/05/21	12.1	1.102	0.22	0.88
0133+476	DA 55	2011/08/18	9.5	1.127	0.29	1.16
0202+319	B2 0202+31	2010/03/07	10.2	0.542	0.16	0.63

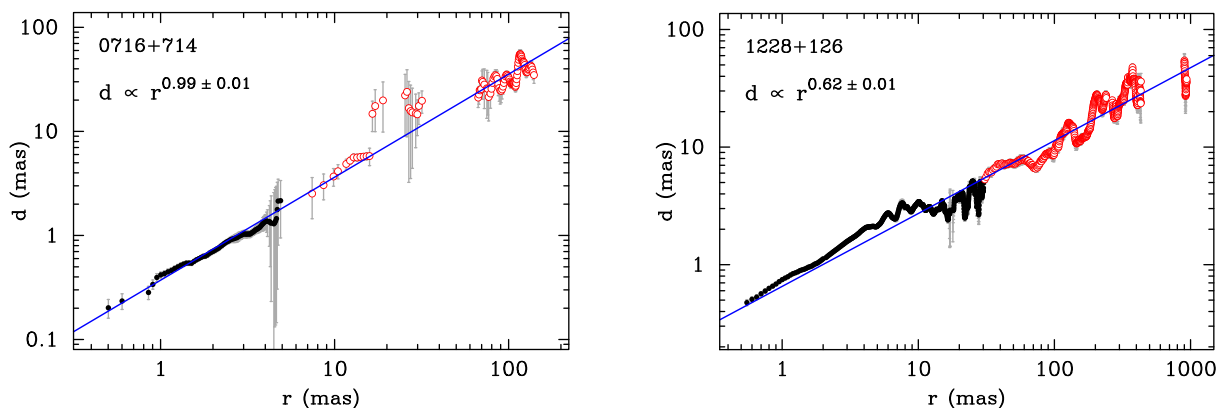


Figure 7. Transverse jet width versus a distance along ridge line for the BL Lac object 0716+714 (left-hand panel) and radio galaxy M87 (right-hand panel) showing conical and parabolic jet shape, respectively, at scales probed by the observations at 15 (filled black dots) and 1.4 GHz (open red circles). The solid blue line is the best fit of an assumed power-law dependence $d \propto r^k$. The plots for other sources are available in the online journal.

we combined the high- and low-frequency (r , d) measurements applying no relative shift in r , but restricting the 1.4 GHz data sets to the distances farther away from the core not covered by the 15 GHz observations. At these outer scales the core shift effect is negligible for the fitting algorithm as it works in a logarithmic scale. In Fig. 7,

we show the combined data sets and corresponding fits. Typically, the truncated 1.4 GHz data at larger scales follow the trend of the 15 GHz measurements quite well, without any essential break in the slope. The BL Lac object 0716+714 (Fig. 7, left-hand panel) shows a conical jet geometry at scales up to 120 mas, corresponding

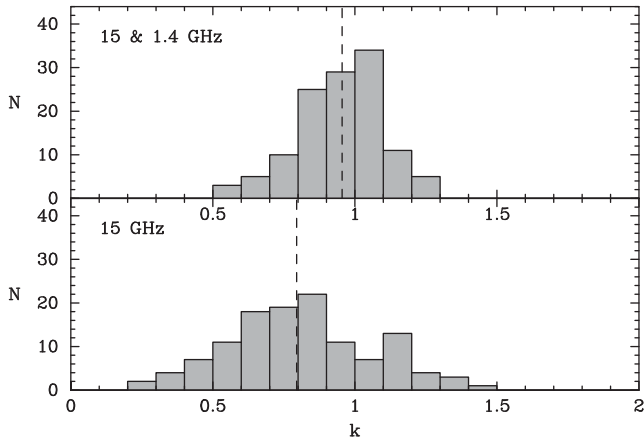


Figure 8. Histograms of the power-law index k in $d \propto r^k$ fitted dependence for 122 MOJAVE-1 sources derived from the 15 GHz data only (bottom panel) and from combined 15 and 1.4 GHz measurements (top panel), with medians of 0.80 and 0.95, respectively, shown by dashed lines.

to about 3 kpc deprojected distance. The radio galaxy M87 (Fig. 7, right-hand panel) manifests a parabolic jet profile with a power-law index k of 0.62 up to scales of 900 mas, where the HST-1 feature is detected, corresponding to deprojected linear distance of 150 pc, assuming viewing angle 30° (Hada et al. 2016). A distribution of k -index derived from the combined data for the 122 MOJAVE-1 sources (Fig. 8, top panel) is narrower and shifted to higher values comparing to those calculated from the 15 GHz data only (Fig. 8, bottom panel). For a subsample of 61 sources with inferred viewing angles, known redshifts and measured projected jet lengths, we calculated the linear deprojected jet lengths, the median of which is about 6 kpc. Thus, the jet shape of the majority of sources from the MOJAVE-1 sample is still close to conical on scales up to a few kpc. We list the jet collimation parameters in Table 4.

An alternative approach to studying jet shape based on measuring VLBI core size and frequency-dependent shift of the core position was successfully used by Nakamura & Asada (2013) and Hada et al. (2013) to investigate the outflow of M87. Application of this method by Algaba et al. (2017) for a sample of 56 radio-loud AGNs observed non-simultaneously in a wide frequency range from 1.6

to 86 GHz showed a diversity of jet geometries, with a typical streamline close to conical.

As it was recently shown by Kovalev, Petrov & Plavin (2017), many AGNs should exhibit prominent parsec-scale jets in the optical band. Since the synchrotron opacity is extremely low at these frequencies, an ability to optically image jets at high angular resolution to probe the jet geometry in the true jet base.

We also note that interstellar scattering resulting in angular broadening is not substantial at 15 GHz (Pushkarev & Kovalev 2015) and therefore should not affect our results. The 1.4 GHz images can be affected by scattering, especially for the sources seen through the Galactic plane, as in the quasar 2005+403 (Fig. 6, right-hand panel). Effects responsible for a severe distortion of the VLBA image of an AGN jet are extremely rare, and have been found by us at 15 GHz for one source only, the quasar 2023+335 (Pushkarev et al. 2013), which is excluded from the analysis of this paper.

3.3 Apparent opening angles

Having measured deconvolved transverse jet widths d at different path lengths r along the ridge line, we calculated the apparent opening angle of the jet as the median value of $\alpha_{\text{app}} = 2 \arctan(0.5d/r)$ for $r > 0.5$ mas, where $d = (D^2 - b^2)^{1/2}$ is the deconvolved FWHM transverse size of the jet, and b is the FWHM size of the restoring beam. In Fig. 9 (top panel), we show a histogram of the derived projected opening angles for all 362 sources. The distribution is broad, comprising values from a few degrees up to 77° for the gamma-ray bright quasar 1520+319, with the median $\alpha_{\text{app}} = 21^\circ.5$. Distributions of α_{app} for BL Lacs and quasars are statistically indistinguishable, with similar medians of $22^\circ.4$ and $21^\circ.1$, respectively. Galaxies show significantly narrower apparent opening angles of their outflows, with a median of $9^\circ.6$, likely due to their statistically larger viewing angles. For the 122 MOJAVE-1 sources observed at 1.4 GHz and having constructed ridgelines, we measured transverse widths and derived apparent opening angles. The latter agree well with α_{app} at 15 GHz, but, on average, are about 10 per cent wider.

Blazar samples are biased in multiple ways (e.g. Vermeulen & Cohen 1994) but using well defined, complete samples can eliminate many of them. Therefore, to make a proper comparison of α_{app} between LAT-detected and non-LAT-detected jets, we used only the sources from the MOJAVE 1.5 Jy (Lister et al. 2015) and 1FM

Table 4. Collimation and kinematic source parameters. Columns are as follows: (1) B1950 name; (2) apparent opening angle at 15 GHz; (3) k -index at 15 GHz; (4) angular jet length along ridgeline at 15 GHz; (5) linear projected jet length at 15 GHz; (6) maximum apparent speed at 15 GHz from Lister et al. (2016); (7) variability Doppler factor from Hovatta et al. (2009) and Liodakis et al. (2017); (8) Lorentz factor; (9) viewing angle; (10) intrinsic opening angle; (11) k -index at 2 GHz; (12) angular jet length along ridgeline at 2 GHz; (13) linear projected jet length at 2 GHz; and (14) linear deprojected jet length at 2 GHz. This table is available in its entirety in the online journal. A portion is shown here for guidance regarding its form and content.

B1950	α_{app}^{15} ($^\circ$)	k_{15}	r_{15} (mas)	l_{15} (pc)	β_{app} (c)	δ	Γ	θ ($^\circ$)	α_{int} ($^\circ$)	k_2	r_2 (mas)	l_2 (kpc)	L_2 (kpc)
(1)	(2)	(3)	(4)	(5)	(6)	(7)	(8)	(9)	(10)	(11)	(12)	(13)	(14)
0003–066	16.5 ± 1.8	0.44 ± 0.03	8.8	42.9	6.15 ± 0.54	5.1 ± 1.3	6.4 ± 0.7	11.1 ± 2.2	3.2 ± 0.7	0.53 ± 0.03	21.3	0.10	0.5
0003+380	27.3 ± 4.3	1.76 ± 0.08	4.9	17.8	–	–	–	–	–	–	–	–	–
0006+061	13.3 ± 2.9	0.69 ± 0.03	22.4	–	–	–	–	–	–	–	–	–	–
0007+106	23.2 ± 3.7	1.91 ± 0.06	1.5	2.5	–	–	–	–	–	–	–	–	–
0010+405	9.3 ± 0.6	0.85 ± 0.07	9.1	35.9	–	–	–	–	–	–	–	–	–
0011+189	15.6 ± 1.1	0.67 ± 0.03	1.9	11.3	–	–	–	–	–	–	–	–	–
0015–054	13.2 ± 1.1	0.52 ± 0.03	2.6	9.3	–	–	–	–	–	–	–	–	–
0016+731	31.0 ± 2.5	1.28 ± 0.02	1.9	16.2	8.22 ± 0.31	7.8 ± 1.9	8.3 ± 0.3	7.4 ± 1.7	4.1 ± 1.0	0.89 ± 0.02	73.7	0.63	4.9
0019+058	43.6 ± 3.8	0.69 ± 0.13	3.5	–	–	–	–	–	–	–	–	–	–
...

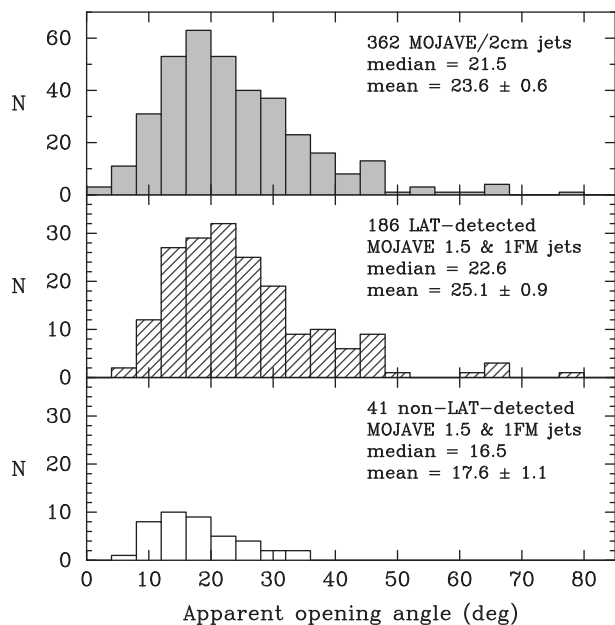


Figure 9. Distributions of the apparent opening angle from jet-cut analysis for all 362 MOJAVE AGNs (top panel), 186 *Fermi* LAT-detected (middle panel) and 41 non-LAT-detected (bottom panel) sources from the MOJAVE 1.5 Jy and 1FM samples.

samples (Lister et al. 2013), representing the brightest radio and gamma-ray AGN jets in the northern sky, respectively. The radio-selected MOJAVE 1.5 Jy sample includes all AGNs (excluding gravitational lenses) with J2000 declination $> -30^\circ$ and VLBA flux density $S_{15\text{GHz}} > 1.5$ Jy at any epoch between 1994.0 and 2010.0. The gamma-ray selected 1FM sample based on the initial 11 month First *Fermi* AGN catalogue (Abdo et al. 2010b) includes all AGNs with an average integrated > 0.1 GeV energy flux $> 3 \times 10^{-11}$ erg cm^{-2} s^{-1} and J2000 declination $> -30^\circ$. Out of 227 sources with measured α_{app} from these two samples, 186 (82 per cent) objects are positionally associated with the gamma-ray bright sources detected by the *Fermi*-LAT during the first 48 months of survey data and included in the third full catalogue (3FGL; Acero et al. 2015) or earlier releases (Abdo et al. 2010a; Nolan et al. 2012). The LAT-detected sources (Fig. 9, middle panel) have statistically wider apparent jet opening angles compared to those of non-LAT-detected (Fig. 9, bottom panel). A Kolmogorov–Smirnov (K-S) test indicates a probability $p = 0.002$ ($p = 0.017$ for 177 sources from the MOJAVE 1.5 Jy sample only), implying that the null hypothesis of the LAT and non-LAT sub-samples coming from the same parent population is rejected. This confirms our earlier findings (Pushkarev et al. 2009) at a much higher level of significance as a result of stronger statistics both in the radio and gamma-ray domains. The LAT-detected AGN jets of the southern sky studied by the TANAMI programme were also found to have wider apparent jet opening angles than non-LAT-detected (Ojha et al. 2010).

We note that all sources with an apparent jet opening angle wider than 35° are LAT-detected. The apparent jet opening angles of the 105 brightest gamma-ray jets (1FM) are found to be wider than those of the 177 brightest radio jets (MOJAVE 1.5 Jy), with medians of $24^\circ.1$ and $20^\circ.2$, respectively. The corresponding distributions are significantly different ($p_{\text{K-S}} = 0.026$).

Our approach of assessing an apparent jet opening angle assumes a conical jet shape, which is not the case for a number of sources (Fig. 5), most noticeably the radio galaxies of the sample, and to

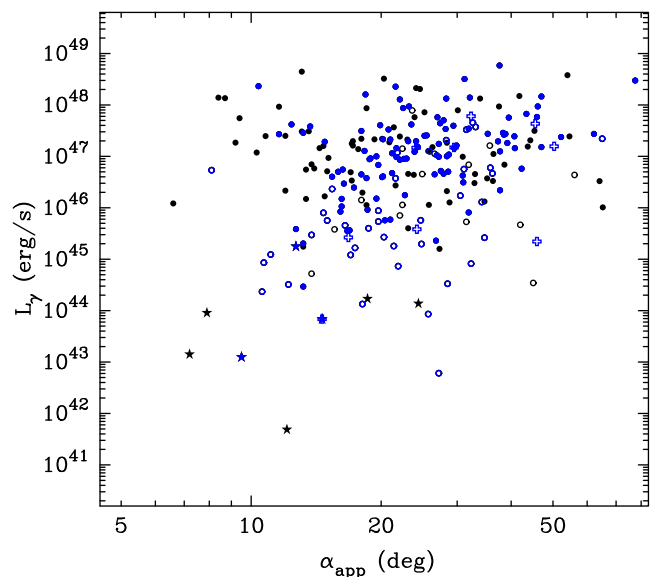


Figure 10. Highly significant correlation between gamma-ray luminosity and apparent jet opening angle for the 250 LAT-detected sources. Filled and empty circles show quasars and BL Lacs, respectively, star symbols denote galaxies, and empty crosses represent optically unidentified sources. The sources with a quasi-conical jet shape are shown by blue.

some extent also a significant number of quasars, that manifest jet profiles close to parabolic, implying a decrease of α_{app} down the jet on scales probed by our observations. For such sources, our method provides an intermediate value of α_{app} , and which may introduce a bias. Therefore, to test this we restricted the calculations to those sources that present a close to conical shape, with $0.7 < k < 1.3$. The obtained distributions and their parameters are close to those from the samples with no jet shape restriction, with an even stronger difference between distributions of α_{app} for the LAT-detected and non-LAT-detected sources ($p = 0.0017$).

We have also established a highly significant correlation (Kendall’s $\tau = 0.2$; $p = 1.6 \times 10^{-5}$), most probably driven by Doppler beaming, between apparent opening angle and gamma-ray luminosity (Fig. 10) derived from 0.1–300 GeV energy fluxes for 250 sources. The correlation remains significant also for different optical classes considered separately. If a sub-sample of sources characterized by quasi-conical jet shapes is considered (Fig. 10, blue colour), the correlation becomes even stronger ($\tau = 0.3$; $p = 10^{-8}$). These findings suggest that the gamma-ray bright AGN jets have, on average, smaller viewing angles (see more detailed analysis in Section 3.4).

As the variation of parsec-scale jet orientation is found to be a common phenomenon for AGNs observed on decadal time-scales (Lister et al. 2013), we studied how this effect influences the measured apparent jet opening angle and how the latter evolves with adding more epochs to the stacked image of a source. For this analysis, we used the data of BL Lac object 1308+326, which is one of 12 MOJAVE sources that manifested oscillatory trends of the innermost jet position angle as reported by Lister et al. (2013). This source did not display a pc-scale jet in the early 1990’s and the opening angle was thus undefined. We therefore used data since the epoch of 2000 January 22, after which the jet was well detected. We made a series of stacked images of the source, continuously adding 54 later epochs until 2015 June 16 inclusive, and measured the apparent opening angle following the procedure described above. The animation of stacked image evolution demonstrates that the

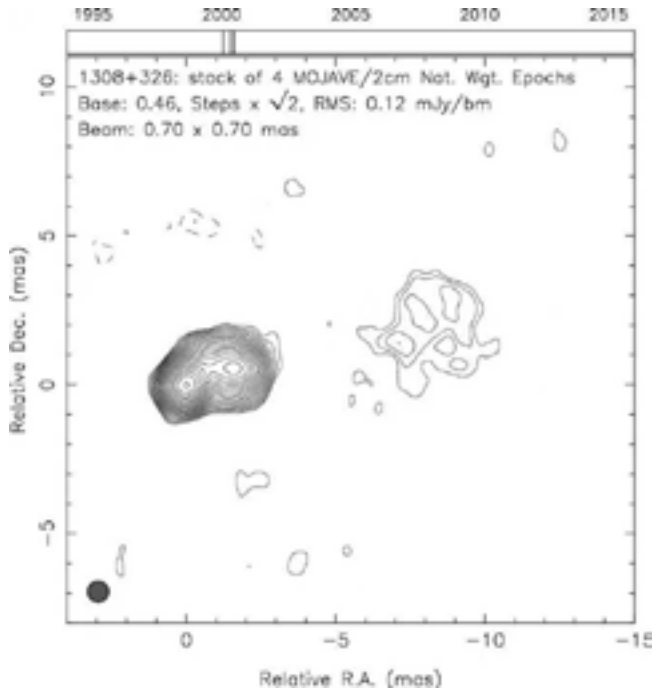


Figure 11. Animated evolution showing the build-up of the stacked image of BL Lac object 1308+326 since the epoch of 2000 January 22, continuously adding 54 later epochs until 2015 June 16.

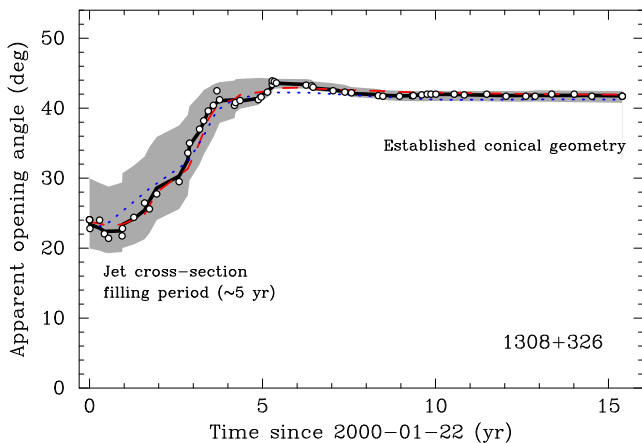


Figure 12. Apparent jet opening angle of BL Lac object 1308+326, as a function of time range in a series of stacked images made with progressively increasing number of epochs (up to 55) since 2000 January 22. The thick curve is constructed by applying a five-point moving average. Grey area indicates the 1σ error level of median apparent opening angles, calculated using bootstrap approach. The dashed red and dotted blue lines represent cases with every second and every third epoch used in stacking, respectively.

jet geometry eventually becomes close to conical (Fig. 11). The corresponding evolution of α_{app} is shown in Fig. 12. The apparent opening angle was of order of 23° until the end of 2000 and then widened to about 40° during about five next years due to emergence of a new bright jet feature in a different position angle, and then α_{app} remains constant. The plateau of α_{app} means that the jet cross-section is effectively filled out by stacking. We performed the same analysis with lower time sampling by using (i) every second and (ii) every third epoch out of the 55 available. In both cases, the obtained dependence of α_{app} versus time range covered by stacking is very close to the original. This implies that the time period of

about 5 yr is not an observation specific bias, but rather a source specific characteristic.

Of course, the duration of the jet cross-section filling period is expected to be source-dependent. To place constraints on this, we studied the dependence between median jet width d_{med} and a number of epochs N in a stacked image for different sets formed by changing minimum time interval Δt covered by stacking, and analysed the corresponding Kendall's correlation statistics. The dependence becomes significant ($p < 0.05$) at $\Delta t \gtrsim 2$ yr, and it is strongest at the minimum time coverage of ~ 6 yr. This implies that an average source changes the inner jet position angle on a time-scale of at least 6 yr. On the other hand, for sources having more than 30 epochs, no significant dependence between d_{med} and N is detected. This corresponds to the time range $\Delta t \gtrsim 16$ yr, setting upper limit on position angle variation time-scale for majority of sources in our sample. This is consistent with indications of oscillatory behaviour of jet orientation with best fitting periods ranging from 5 to 12 yr found by Lister et al. (2013).

3.4 Intrinsic opening angles and viewing angles

The intrinsic jet opening angles can be calculated as $\tan(\alpha_{\text{int}}/2) = \tan(\alpha_{\text{app}}/2) \sin \theta$, where θ is the viewing angle to the jet axis. The latter, as well as the bulk Lorentz factor Γ , can be derived from apparent jet speed and Doppler factor using the following relations:

$$\theta = \arctan \frac{2\beta_{\text{app}}}{\beta_{\text{app}}^2 + \delta_{\text{var}}^2 - 1}, \quad \Gamma = \frac{\beta_{\text{app}}^2 + \delta_{\text{var}}^2 + 1}{2\delta_{\text{var}}}.$$

For β_{app} and δ_{var} we used the fastest measured radial, non-accelerating apparent jet speed from the MOJAVE kinematic analysis (Lister et al. 2016) and the variability Doppler factor from the Metsähovi AGN monitoring programme (Hovatta et al. 2009), respectively. The corresponding overlap of the programmes comprises 55 sources, which are all members of the MOJAVE-1 sample. Variability Doppler-factors for 10 more MOJAVE-1 sources were measured within the F-GAMMA programme (Liodakis et al. 2017). The intrinsic opening angles calculated for the 65 sources range from $0^\circ.1$ to $9^\circ.4$, with a median of $1^\circ.3$, reflecting a very high degree of jet collimation. The intrinsic opening angles show an inverse dependence on Lorentz factor (Fig. 13), as predicted by hydrodynamical (Blandford & Königl 1979) and magnetic acceleration models (Komissarov et al. 2007) of relativistic jets. The median value of the product³ $\rho = \alpha_{\text{int}}\Gamma$ is 0.35 rad, close to earlier estimates derived both from observations (Jorstad et al. 2005; Pushkarev et al. 2009) and from a statistical model approach (Clausen-Brown et al. 2013). The variability Doppler factors derived from variability can be underestimated due to a limited cadence of the observations. In this case, the intrinsic opening angle estimates would be smaller, while Lorentz factors would be higher if $\delta > (\beta_{\text{app}}^2 + 1)^{1/2}$ and smaller otherwise, implying that if the variability Doppler factors are essentially underestimated, the majority of points in Fig. 13 would move downward and to the right.

The LAT-detected AGNs have statistically narrower jets than non-LAT-detected, with medians of $\alpha_{\text{int}}^{\text{LAT}} = 1^\circ.2$ and $\alpha_{\text{int}}^{\text{non-LAT}} = 2^\circ.5$, respectively. We have found no significant difference in α_{int} between

³ As we use the full opening angle, ρ in this paper is not defined the same way as ρ in Jorstad et al. (2005) and Clausen-Brown et al. (2013), but they differ by a factor of 2.

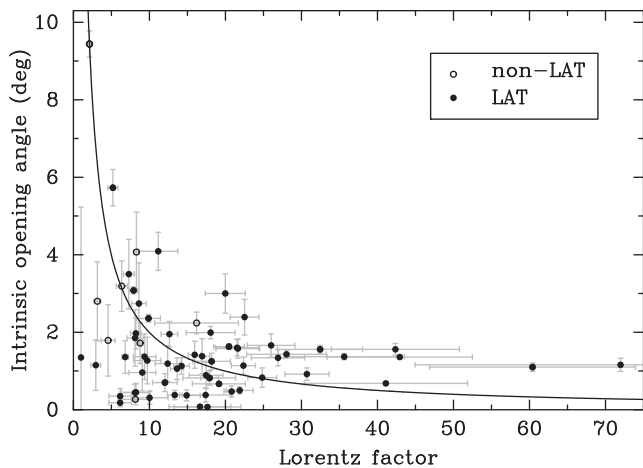


Figure 13. Intrinsic opening angle versus Lorentz factor for 65 AGN jets. The solid line shows the median curve fit with the assumed relation $\alpha_{\text{int}} = \rho/\Gamma$, where ρ is a constant (here $\rho = 0.35$ rad). Filled and open circles represent LAT-detected and non-LAT-detected sources, respectively.

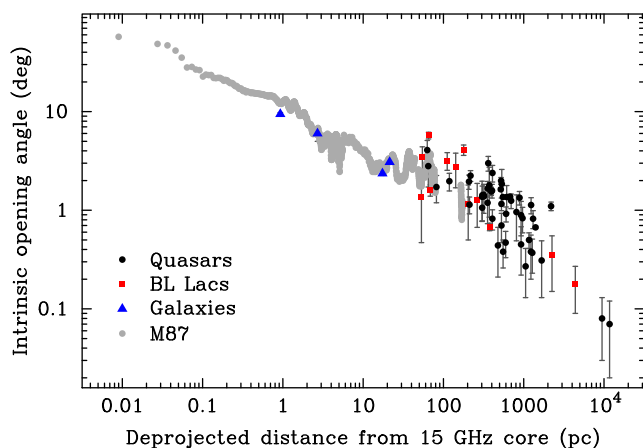


Figure 14. Intrinsic opening angle versus median distance from the 15 GHz core for the 65 AGN jets with viewing angle estimates (Table 4). Galaxies, BL Lacs, and quasars are shown by blue triangles, red squares and black circles, respectively. Grey points represent M87 (same data as in Fig. 7, right-hand side) to cover small scales.

quasars and BL Lacs. The geometry and kinematics jet parameters are listed in Table 4.

In Fig. 14, we plot the intrinsic jet opening angles against deprojected median distance from the 15 GHz core for the 65 sources supplemented by a scan along the jet of M87 (to trace small scales). It shows a trend from a very wide-opened outflow near the jet apex through an acceleration zone (Homan et al. 2015; Lister et al. 2016) to highly collimated jet regions on kiloparsec scales, with opening angles of the order of 1° or even narrower. Jet shapes at different scales and their transitions will be discussed in Kovalev et al. (in preparation).

The jet viewing angle can be expressed as

$$\theta = \text{asin} \left(\frac{\tan(0.5\rho/\Gamma)}{\tan(0.5\alpha_{\text{app}})} \right) \approx \text{asin} \left(\frac{\tan(0.5\rho/\sqrt{\beta_{\text{app}}^2 + 1})}{\tan(0.5\alpha_{\text{app}})} \right),$$

where the latter approximation assumes $\theta \simeq 1/\Gamma$. We used Monte Carlo simulations to construct the viewing angle distributions separately for the LAT and non-LAT sub-samples, assuming flat distri-

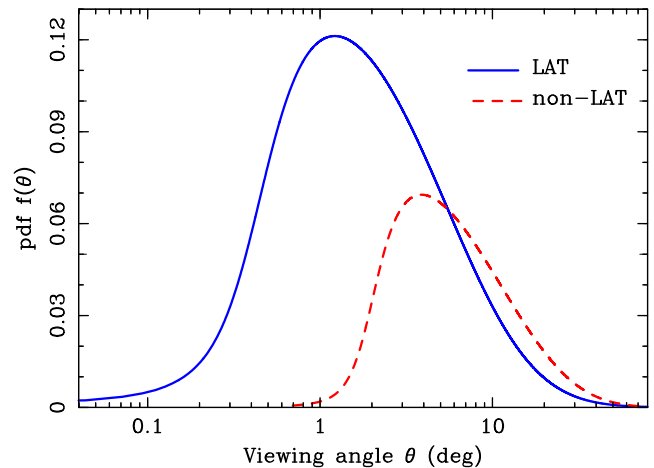


Figure 15. Probability density functions of jet viewing angle for the *Fermi* LAT-detected (solid blue line) and non-LAT-detected (dashed red line) AGNs, with medians of 6° and 11° , respectively.

butions for ρ in the ranges $[0.05, 1.0]$ and $[0.2, 0.6]$, respectively. The quantile functions of α_{app} and β_{app} needed for the simulations were obtained in a closed form by applying the Generalized Lambda Distribution (GLD; King & MacGillivray 1999) technique to fit the original distributions. For β_{app} we used the fastest radial, non-accelerating apparent jet speeds measured by the MOJAVE programme to date (Lister et al. 2016).

Applying the method of maximum likelihood and RS-parametrization of the GLD (Ramberg & Schmeiser 1974), we have constructed probability density functions (PDFs) of the simulated viewing angle distributions for the LAT-detected and non-LAT-detected sources (Fig. 15). The inferred PDFs have shapes close to lognormal and clearly show that jets of the gamma-ray bright AGNs tend to have statistically smaller angles to the line of sight comparing to those of gamma-ray weak AGNs, with median values 6° and 10° , respectively. At $\theta \approx 5^\circ$, the probability of detecting gamma-ray weak source is becoming higher than that of gamma-ray bright AGN, and a ratio of the corresponding probabilities increases towards the right tail of the θ distributions. Statistically, the probability to observe a LAT-detected source within the jet cone with a typical $\alpha_{\text{int}} \approx 1^\circ$ is about 1.5 per cent, corresponding to three sources in a sub-sample of 186 objects. The quasar 1520+319 (showing the widest $\alpha_{\text{app}} = 77^\circ$) might be one of such cases.

We note that it is unclear whether the assumption that LAT and non-LAT-detected sources have the same relation between the viewing angle and Lorentz factor ($\theta \simeq 1/\Gamma$) introduces some bias in the calculation of the probability density functions of the jet viewing angle. As discussed by Lister et al. (2015), many AGN have not been detected by the *Fermi*-LAT partly because of an instrumental selection effect and partly due to their lower Doppler boosting factors. This in some degree justifies using the same assumption for LAT-detected and non-LAT-detected sources. At the same time, it was shown that the approximation $\theta \simeq 1/\Gamma$ could be less correct for jets with lower Lorentz factor and/or larger viewing angle (Lister 1999), as it is often the case for non-LAT-detected AGNs.

4 CONCLUSIONS

We have produced total intensity stacked images at 15 GHz for 370 AGN jets having at least five epochs of observations within the MOJAVE programme or 2-cm VLBA Survey, and constructed the

corresponding ridgelines along the outflows. Analysing projected jet width at different separations from the VLBA core for 360 sources at 15 GHz, we have found that jets of quasars and BL Lacs typically show a geometry close to conical, while radio galaxies manifest streamlines closer to parabolic. The AGN jets with significant radial accelerated motion undergo more active collimation. Jets are conical at larger, up to a few kpc, scales probed by the 1.4 GHz VLBA observations.

By making cuts transverse to the local jet direction, we have measured widths and projected jet opening angles on parsec scales for 362 sources (282 LAT-detected and 80 non-LAT-detected). The apparent opening angles for γ -ray bright sources are, on average, larger than those in γ -ray weak ones, with medians of 23° and 15° , respectively. All AGNs with an apparent jet opening angle wider than 35° are LAT-detected. We have established a highly significant correlation between the apparent opening angle and gamma-ray luminosity, driven by Doppler beaming. We find that in many cases, a conical jet geometry only emerges after numerous images spanning several years are stacked together. A significant dependence is detected between the median jet width and a minimum time interval of epochs Δt in a stacked image if Δt ranges from 2 to 16 yr, with the strongest correlation at $\Delta t \gtrsim 6$ yr, which is consistent with indications of oscillatory behaviour of jet orientation with fitted periods ranging from 5 to 12 yr found by Lister et al. (2013). On larger scales, probed by the single-epoch 1.4 GHz VLBA observations of a sub-sample of 122 MOJAVE sources, apparent opening angles agree well with those at 15 GHz, but on average are about 10 per cent wider.

The intrinsic opening angles calculated for a sample of 65 AGNs (i) range from 9.4° at scales of the order of 1 pc down to 0.1° at kiloparsec scales with a median of 1.3° , reflecting very high degree of jet collimation; and (ii) show inverse dependence on Lorentz factor with a median product $\Gamma\alpha_{\text{int}} = 0.35$ rad. The LAT-detected AGNs have statistically narrower jets than non-LAT-detected, with medians of $\alpha_{\text{int,LAT}_Y} = 1.2^\circ$ and $\alpha_{\text{int,LAT}_N} = 2.5^\circ$. We have found no significant difference in α_{int} between quasars and BL Lacs. Performing Monte Carlo simulations, we have constructed viewing angle distributions and showed that the gamma-ray bright AGNs have statistically smaller angles to the line of sight comparing to those of gamma-ray weak sources, with median values 6° and 10° , respectively.

ACKNOWLEDGEMENTS

We thank the anonymous referee for useful comments that helped to improve the manuscript. This research has made use of data from the MOJAVE data base, which is maintained by the MOJAVE team (Lister et al. 2009a). The MOJAVE project was supported by NASA-*Fermi* GI grants NNX08AV67G, NNX12A087G and NNX15AU76G. This study was supported by the Russian Foundation for Basic Research grant 15-42-01020. TS was funded by the Academy of Finland projects 274477 and 284495. The National Radio Astronomy Observatory is a facility of the National Science Foundation operated under cooperative agreement by Associated Universities, Inc.

REFERENCES

Abdo A. A. et al., 2010a, *ApJS*, 188, 405
 Abdo A. A. et al., 2010b, *ApJ*, 715, 429
 Acero F. et al., 2015, *ApJS*, 218, 23
 Algaba J. C., Nakamura M., Asada K., Lee S. S., 2017, *ApJ*, 834, 65

Asada K., Nakamura M., 2012, *ApJ*, 745, L28
 Blandford R. D., Königl A., 1979, *ApJ*, 232, 34
 Boccardi B., Krichbaum T. P., Bach U., Mertens F., Ros E., Alef W., Zensus J. A., 2016, *A&A*, 585, A33
 Böttcher M. et al., 2005, *ApJ*, 631, 169
 Cara M., Lister M. L., 2008, *ApJ*, 674, 111
 Clausen-Brown E., Savolainen T., Pushkarev A. B., Kovalev Y. Y., Zensus J. A., 2013, *A&A*, 558, A144
 Cohen M. H., Lister M. L., Homan D. C., Kadler M., Kellermann K. I., Kovalev Y. Y., Vermeulen R. C., 2007, *ApJ*, 658, 232
 Cooper N. J., Lister M. L., Kochanzyk M. D., 2007, *ApJS*, 171, 376
 Giroletti M., Giovannini G., Cotton W. D., Taylor G. B., Pérez-Torres M. A., Chiaberge M., Edwards P. G., 2008, *A&A*, 488, 905
 Hada K., Doi A., Kino M., Nagai H., Hagiwara Y., Kawaguchi N., 2011, *Nature*, 477, 185
 Hada K. et al., 2013, *ApJ*, 775, 70
 Hada K. et al., 2016, *ApJ*, 817, 131
 Homan D. C., Lister M. L., 2006, *AJ*, 131, 1262
 Homan D. C., Kadler M., Kellermann K. I., Kovalev Y. Y., Lister M. L., Ros E., Savolainen T., Zensus J. A., 2009, *ApJ*, 706, 1253
 Homan D. C., Lister M. L., Kovalev Y. Y., Pushkarev A. B., Savolainen T., Kellermann K. I., Richards J. L., Ros E., 2015, *ApJ*, 798, 134
 Hovatta T., Valtaoja E., Tornikoski M., Lähteenmäki A., 2009, *A&A*, 498, 723
 Hovatta T., Lister M. L., Aller M. F., Aller H. D., Homan D. C., Kovalev Y. Y., Pushkarev A. B., Savolainen T., 2012, *AJ*, 144, 105
 Hovatta T. et al., 2014, *AJ*, 147, 143
 Jones D. H., Saunders W., Read M., Colless M., 2005, *PASA*, 22, 277
 Jorstad S. G. et al., 2005, *AJ*, 130, 1418
 Junor W., Biretta J. A., Livio M., 1999, *Nature*, 401, 891
 Kadler M., Ros E., Lobanov A. P., Falcke H., Zensus J. A., 2004, *A&A*, 426, 481
 Kellermann K. I., Pauliny-Toth I. I. K., 1969, *ApJ*, 155, L71
 Kellermann K. I., Vermeulen R. C., Zensus J. A., Cohen M. H., 1998, *AJ*, 115, 1295
 King R., MacGillivray H., 1999, *Aust. N.Z. J. Stat.*, 41
 Komatsu E. et al., 2009, *ApJS*, 180, 330
 Komissarov S. S., Barkov M. V., Vlahakis N., Königl A., 2007, *MNRAS*, 380, 51
 Kovalev Y. Y., Lobanov A. P., Pushkarev A. B., Zensus J. A., 2008, *A&A*, 483, 759
 Kovalev Y. Y., Petrov L., Plavin A. V., 2017, *A&A*, 598, L1
 Kravchenko E. V., Kovalev Y. Y., Hovatta T., Ramakrishnan V., 2016, *MNRAS*, 462, 2747
 Kutkin A. M. et al., 2014, *MNRAS*, 437, 3396
 Lawrence C. R., Pearson T. J., Readhead A. C. S., Unwin S. C., 1986, *AJ*, 91, 494
 Lioudakis I. et al., 2017, *MNRAS*, 466, 4625
 Lister M. L., 1999, PhD thesis, Univ. Boston
 Lister M. L., Homan D. C., 2005, *AJ*, 130, 1389
 Lister M. L. et al., 2009a, *AJ*, 137, 3718
 Lister M. L. et al., 2009b, *AJ*, 138, 1874
 Lister M. L. et al., 2011, *ApJ*, 742, 27
 Lister M. L. et al., 2013, *AJ*, 146, 120
 Lister M. L., Aller M. F., Aller H. D., Hovatta T., Max-Moerbeck W., Readhead A. C. S., Richards J. L., Ros E., 2015, *ApJ*, 810, L9
 Lister M. L. et al., 2016, *AJ*, 152, 12
 Lobanov A. P., 1998, *A&A*, 330, 79
 Nakamura M., Asada K., 2013, *ApJ*, 775, 118
 Nolan P. L. et al., 2012, *ApJS*, 199, 31
 Ojha R. et al., 2010, *A&A*, 519, A45
 Pushkarev A. B., Kovalev Y. Y., 2012, *A&A*, 544, A34
 Pushkarev A. B., Kovalev Y. Y., 2015, *MNRAS*, 452, 4274
 Pushkarev A. B., Kovalev Y. Y., Lister M. L., Savolainen T., 2009, *A&A*, 507, L33
 Pushkarev A. B., Hovatta T., Kovalev Y. Y., Lister M. L., Lobanov A. P., Savolainen T., Zensus J. A., 2012, *A&A*, 545, A113
 Pushkarev A. B. et al., 2013, *A&A*, 555, A80

- Ramberg J., Schmeiser B., 1974, *Commun. Assoc. Explor. Geophys.*, 17, 78
- Rau A. et al., 2012, *A&A*, 538, A26
- Sargent W. L. W., 1970, *ApJ*, 160, 405
- Savolainen T., Wiik K., Valtaoja E., Kadler M., Ros E., Tornikoski M., Aller M. F., Aller H. D., 2006, *ApJ*, 647, 172
- Shaw M. S. et al., 2012, *ApJ*, 748, 49
- Shaw M. S. et al., 2013, *ApJ*, 764, 135
- Shepherd M. C., 1997, in Hunt G., Payne H. E., eds, *ASP Conf. Ser. Vol. 125, Astronomical Data Analysis Software and Systems VI*. Astron. Soc. Pac., San Francisco, p. 77
- Sokolovsky K. V., Kovalev Y. Y., Pushkarev A. B., Lobanov A. P., 2011, *A&A*, 532, A38
- Stickel M., Kuehr H., 1994, *A&AS*, 103
- Thompson D. J., Djorgovski S., Vigotti M., Grueff G., 1992, *ApJS*, 81, 1
- Tseng C.-Y., Asada K., Nakamura M., Pu H.-Y., Algaba J.-C., Lo W.-P., 2016, *ApJ*, 833, 288
- Vermeulen R. C., Cohen M. H., 1994, *ApJ*, 430, 467
- Zensus J. A., Ros E., Kellermann K. I., Cohen M. H., Vermeulen R. C., Kadler M., 2002, *AJ*, 124, 662

SUPPORTING INFORMATION

Supplementary data are available at [MNRAS](#) online.

Table 1. Source properties.

Table 2. Summary of 15 GHz stacked image parameters.

Table 3. Summary of 1.4 GHz single-epoch image parameters.

Table 4. Collimation and kinematic source parameters.

Figure 2. 15 GHz naturally weighted stacked VLBA contour images of observed 362 sources. The contours are plotted at increasing powers of $\sqrt{2}$. The restoring beam is depicted as a shaded circle in the lower left corner. The constructed total intensity ridgeline is shown by red. A wedge indicating observing epochs (vertical ticks) used for producing the stacked image is shown on top.

Figure 4. Transverse jet width versus a distance along ridge line for BL Lac at scales probed by the MOJAVE observations at 15 GHz.

Figure 6. Naturally weighted 1.4 GHz VLBA contour images of 122 MOJAVE-1 sources. The contours are plotted at increasing powers of $\sqrt{2}$. The restoring beam is depicted as a shaded circle in the lower left corner. Constructed total intensity ridgeline is shown by red.

Figure 7. Transverse jet width versus a distance along ridge line for the BL Lac object 0716+714 (left panel) and radio galaxy M87 (right panel) showing conical and parabolic jet shape, respectively, at scales probed by the observations at 15 (filled black dots) and 1.4 GHz (open red circles)

Please note: Oxford University Press is not responsible for the content or functionality of any supporting materials supplied by the authors. Any queries (other than missing material) should be directed to the corresponding author for the article.

This paper has been typeset from a $\text{\TeX}/\text{\LaTeX}$ file prepared by the author.